Catalysis Science & Technology

PAPER

Cite this: *Catal. Sci. Technol.*, 2016, 6, 6845

Design and synthesis of model and practical palladium catalysts using atomic layer deposition†

Zheng Lu,[a] Orhan Kizilkaya,[b] A. Jeremy Kropf,[c] Mar Piernavieja-Hermida,[a] Jeffrey T. Miller,[cd] Richard L. Kurtz,[be] Jeffrey W. Elam*[f] and Yu Lei*[a]

Received 29th March 2016,
Accepted 4th May 2016

DOI: 10.1039/c6cy00682e

www.rsc.org/catalysis

We investigated the "one-batch" synthesis of model and practical palladium catalysts using atomic layer deposition (ALD). Two types of model catalysts and one type of powder-based nanocatalyst were synthesized simultaneously by ALD under viscous flow conditions. In addition, Pd/TiO_2(110) model catalysts were prepared by the identical ALD process but under ultrahigh vacuum conditions. Because of the self-limiting surface reaction that defines ALD, the local structure of all the Pd catalysts were essentially the same as confirmed by a suite of microscopic and spectroscopic characterization techniques. A comprehensive understanding of the Pd-based catalysts was achieved by applying both surface science probes and advanced synchrotron techniques, and by strategically selecting the catalyst substrate best suited for each characterization. Both X-ray absorption spectroscopy and X-ray resonant photoelectron spectroscopy suggested that Pd only weakly interacted with the TiO_2 support. The one-batch synthesis approach facilitated by ALD can potentially bridge the "synthesis gap" between model catalysts and practical catalysts.

Introduction

Catalytic reactions are complicated in that their selectivity and conversion can be affected by many factors which range from interactions at the atomic level to heat and mass transport in the reactor which may operate on the scale of tons. For fundamental studies, it is necessary to reduce the number of these variables to a tractable level. Therefore, well-defined metal single crystals have often been used as model systems under ultrahigh vacuum (UHV) conditions to establish structure/activity relationships and identify active sites.[1,2]

A common criticism of the single crystal approach to catalysis research is that several important factors which influence reactivity are not present including the catalyst particle size effect and the influence of the support. Therefore, in the mid-to-late 1990,[3–6] efforts were made to bridge the "materials gap" by depositing metal particles on planar metal oxides which are designed to mimic the support.

Scheme 1 shows a well-defined model catalyst composed of three parts: 1. A single crystal substrate, 2. A crystalline or amorphous metal oxide support thin film grown on the single crystal substrate, and 3. Metal clusters and nanoparticles which are deposited onto the oxide support. In some model catalyst studies, the system may consist of only two (or even one) of the components. For example, metal nanoparticles may be supported by a single crystal surface[7] or the catalyst may be the metal oxide thin film itself.[8] A typical method to prepare the thin oxide support film and the nanoparticles suitable for surface science studies is to grow these materials *via* physical vapor deposition (PVD) of the corresponding metal under UHV conditions.

Although planar model catalysts lack the complexity of high surface area industrial catalysts, they provide several

[a] *Department of Chemical and Materials Engineering, University of Alabama in Huntsville, Huntsville, AL, 35899 USA. E-mail: yu.lei@uah.edu*
[b] *Center for Advanced Microstructures and Devices, Louisiana State University, Baton Rouge, LA, 70806 USA*
[c] *Chemical Sciences and Engineering Division, Argonne National Laboratory, Lemont, IL, 60439 USA*
[d] *School of Chemical Engineering, Purdue University, West Lafayette, IN, 47907 USA*
[e] *Department of Physics and Astronomy, Louisiana State University, Baton Rouge, LA, 70803 USA*
[f] *Energy Systems Division, Argonne National Laboratory, Lemont, IL, 60439 USA. E-mail: jelam@anl.gov*

† Electronic supplementary information (ESI) available: AFM image, XAS spectra. See DOI: 10.1039/c6cy00682e

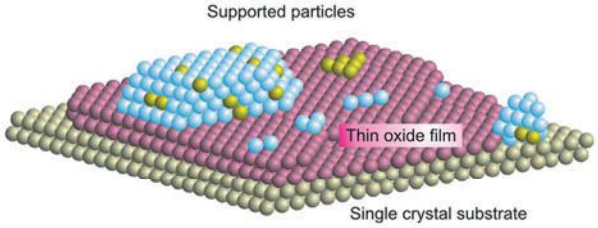

Scheme 1 Supported model catalyst (from bottom to top): I. single crystal substrate (gold), II. thin oxide film (red), III. supported particles (blue and yellow).

advantages for catalyst research: 1) as mentioned above, since the oxide films utilized in model catalysis studies are thin, they can often permit electron tunneling, so that tools such as scanning tunneling microscopy (STM) may be employed to characterize the catalyst structure (both geometric and electronic) in great detail and to identify the adsorption sites of probe molecules; 2) The number of parameters involved in model catalysis studies is relatively small, which allows direct comparison between experimental and theoretical results. Despite the simplifying assumptions associated with planar model catalysts, compared with either gas phase cluster studies[9] or metal single crystal studies, investigations over model catalysts involving supported nanoparticles on planar substrates are a critical step forward toward practical catalysts.

Model catalysis systems have been intensively studied in the past decades. However, it is sometimes difficult to directly compare practical catalysts with model catalysts due to the much different fabrication methods for these two types of catalyst. Practical catalysts are typically prepared by chemical methods involving the presence of water or moisture (*e.g.*, precipitation, impregnation, sol–gel, CVD, *etc.*) while the well-defined model catalysts are prepared by physical approach on a clean surface with little to no surface water (*i.e.*, under UHV conditions). The different synthesis methods may lead to catalysts with different morphologies and compositions. This makes it challenging to directly apply the discoveries from well-defined model catalysts to practical catalysis systems. Bridging this "synthesis gap" requires an efficient way to prepare identical oxide thin films and nanoparticles on both planar substrates and high surface area materials. Moreover, the ability to scale-up practical applications is highly desirable.

Efforts have been dedicated to bridge the pressure gap and materials gap between surface science and practical catalysis studies.[10–14] Although PVD has been the major method to prepare model catalysts under UHV conditions for surface science studies, it is difficult for PVD to provide conformal coatings of metal nanoparticles and metal oxide thin films on high aspect ratio substrates, making it unfeasible to synthesize industrial catalysts where high surface area powders are used as support materials. On the other hand, wet impregnation (WI) has been an inexpensive, rapid and popular method to prepare industrial catalysts. To bridge the gap of materials synthesis, Sterrer and coworkers recently utilized WI to synthesize Pd nanoparticles on well-defined oxide single crystal surfaces to enable surface science studies.[15,16] The approach required transferring a clean single crystal out of the UHV chamber for WI of Pd nanoparticles, and subsequently studying the surface structure using microscopic and spectroscopic techniques.

Atomic Layer deposition (ALD) by means of sequential exposure of gas phase chemicals (precursors), is a promising technique for producing conformal coatings of thin oxide films and uniform metal nanoparticles.[17–22] Due to its unique feature of self-limiting surface reactions, it is feasible to produce identical catalysts on both planar substrates and high surface area materials. ALD has been employed to prepare alumina thin films as supports for model silver catalysts[23] and as protecting layers for practical palladium catalysts.[24] As a vacuum-based technique, both model and powder catalysts can be prepared simultaneously in the vacuum chamber, eliminating the possibility of contamination due to sample transfer. In addition, ALD can also be carried out in fluidized bed reactors for the large scale production of industrial catalysts.[25] Consequently, ALD is a promising strategy to bridge the "synthesis gap" between model catalysts and practical catalysts.

Extending our previous work preparing Pd nanocatalysts on model[26] and practical catalysts,[27,28] we prepared identical Pd nanocatalysts on TiO_2-coated fused silica plates, TiO_2-coated Si(100) wafers and TiO_2(110) single crystals as model catalysts. We utilized both surface science probes on model catalysts and conventional characterization on practical catalysts. The first part of this work uses characterization techniques that can be applied to all samples under similar conditions. This part of the work aims at demonstrating the ALD samples are similar with respect Pd particle size, oxidation state, and surface composition regardless of the substrate. The second part of the work employs techniques that can only be used to measure samples with certain restrictions, *e.g.*, grazing incidence X-ray absorption spectroscopy has difficulty in measuring samples with crystalline substrates and X-ray photoelectron spectroscopy prefers substrates that are conductive. As each characterization technique has its own limitation, the ability to prepare identical model and practical catalysts on a variety of substrates simultaneously using ALD under the same conditions, allows us to obtain a comprehensive understanding of the catalyst behavior.

Experimental

Catalyst Preparation

Model catalysts Pd/TiO_2/Si(100) and Pd/TiO_2/fused silica and practical catalysts Pd/TiO_2/SiO_2 gel were prepared simultaneously in a viscous flow hot-walled ALD system that has been described in detail elsewhere.[29] High purity polished fused silica plates (Technical Glass Products) and Si(100) wafers (SQI, Inc) were used as substrates for model catalysts. The optically smooth fused silica plates have a thickness of 1 mm. The N-type high conductive Si(100) wafer has resistivity of less than 0.005 ohm cm and thickness of 0.5 mm. The Si(100) wafer is covered by 17 Å of native SiO_2 measured by spectroscopic ellipsometry. The SiO_2 gel used in this work was Silicycle S10040 M silica gel with ~100 m^2 g^{-1} surface area, a particle size of 75–200 μm, and a pore diameter of 30 nm. 0.5 g of the pre-baked SiO_2 gel was uniformly spread onto a stainless steel sample plate with a mesh top. The stainless steel sample plate was held on a stainless steel sample tray that also supported the Si(100) and fused silica wafers. The wafer samples and powder plate were loaded into the center of the reactor and kept for at least 30 minutes at

200 °C in a 350 sccm flow of UHP N_2 at 1 Torr pressure to allow temperature stabilization and further outgassing the SiO_2 gel. Next, the samples were cleaned *in situ* using 30 sccm of flowing ozone (10% O_3 in O_2) at 1 Torr pressure at 200 °C for 15 minutes. After cleaning, the substrates were coated using TiO_2 ALD. The TiO_2 ALD used alternating exposures to $TiCl_4$ (Sigma-Aldrich, 99.9%) and deionized water at 150 °C. Next, ALD Pd nanoparticles were deposited on top of the ALD TiO_2 support layer. The Pd ALD used alternating exposures to palladium hexafluoroacetylacetonate ($Pd(hfac)_2$, Sigma-Aldrich, 99.9%) and formalin (Sigma-Aldrich, HCHO 37 wt% in H_2O) at 200 °C.[30]

The Pd/TiO_2(110) model catalysts were studied in a UHV system equipped with an Omicron variable-temperature STM and low-energy electron diffraction (LEED) under a base pressure of 1×10^{-10} mbar. A new rutile TiO_2(110) single crystal (Crystal GmbH, $10 \times 10 \times 1.0$ mm^3) was repeatedly sputter-cleaned and annealed to 900 K in the preparation chamber to prepare a clean TiO_2(110) surface. $Pd(hfac)_2$ was introduced at 373 K to deposit a sub-monolayer of adsorbed Pd(hfac)* species on the TiO_2(110) surface. Next, the surface was heated to 700 K in UHV to thermally decompose the adsorbed Pd(hfac)* and produce the Pd/TiO_2(110) catalyst.

Catalyst Characterization

X-ray absorption spectroscopy (XAS), including extended X-ray absorption fine structure spectroscopy (EXAFS) and X-ray absorption near edge structure spectroscopy (XANES), was conducted at the beamline of the Materials Research Collaborative Access Team (MRCAT) at Sector 10-ID of the Advanced Photon Source, Argonne National Laboratory. Spectra at the Pd K edge (24.35 keV) were acquired for the samples. Pd foil was used to calibrate the monochromator. The samples were fully reduced using 50 sccm 3.5% H_2 in He as balance gas at 523 K for one hour. Next, the reactor was purged using 150 sccm ultrahigh purity He for 10 minutes at 523 K. The samples were cooled to room temperature in He and measured as the "reduced" sample to obtain precise information on the metal–metal bond distances and coordination numbers and to facilitate determination of the particle structure and size.

The XAS measurements were carried out in transmission mode for the Pd/TiO_2/SiO_2 gel powder catalysts. Grazing-incident XAS was performed for the Pd/TiO_2/fused silica model catalyst with an incident angle 0.16°, which is below the critical angle of SiO_2 (0.20°). A Lytle detector was used for collecting the florescence signal from the sample. The model catalysts were treated under the same conditions as described for powder catalysts.

Standard procedures based on WINXAS 3.1 software were used to fit the data in the EXAFS regime.[31] The Pd–Pd scattering phase shift and amplitude were obtained from reference Pd foil for Pd–Pd (N_{Pd-Pd} = 12 at 2.75 Å). A two-shell model fit of the k^2-weighted EXAFS data was obtained between k = 2.8–11.5 Å^{-1} and r = 1.3–3.0 Å, respectively.

X-ray resonant photoemission spectroscopy (RPES) was performed at the 3 m toroidal grating monochromator (TGM) beamline at Center for Advanced Microstructures and Devices (CAMD) at Louisiana State University. The beamline is equipped with a photoemission endstation using a 50 mm hemispherical electron energy analyzer. The Pd/TiO_2/SiO_2/Si(100) model catalyst was placed on a Ta sheet which was resistively heated. The sample was first slowly degassed in the UHV chamber at 523 K. Next, the sample was continuously reduced by back-filling the UHV chamber with 5×10^{-5} mbar ultrahigh purity hydrogen at 523 K for 30 minutes. Finally, the sample was slowly cooled down to room temperature in UHV. The valence band was acquired from the hydrogen reduced samples with different photon energies in the range 34–110 eV.

Scanning transmission electron microscopy (STEM) and atomic number contrast high angle annular dark field (HAADF) imaging was performed using a probe aberration corrected 200 kV JEOL JEM-ARM200CF STEM/TEM with a resolution of less than 0.08 nm at Research Resources Center at University of Illinois at Chicago. The histogram of particle size distribution was generated from the STEM images using ImageJ software.[32] X-ray photoelectron spectroscopy (XPS) was performed using a Kratos AXIS-165 system equipment with a monochromatic Al K_α (1486.6 eV) X-ray source operating at 15 kV and 10 mA. A charge neutralizer was used to compensate the charging effect when the Pd/TiO_2/SiO_2 gel catalyst was measured. The spectral line of C 1s (284.6 eV) was used for the normalization of the binding energy. X-ray diffraction (XRD) was performed using a Rigaku MiniFlex 600 powder X-ray diffractometer operated at 40 kV and 15 mA; 2 theta data from 0° to 90° were obtained at scanning speeds of 0.5°/min.

Results and discussion

The catalysts used in this work can be described by three components: substrate, metal oxide support layer and Pd nanoparticles. Here, the substrates, *i.e.*, fused silica, Si(100) and SiO_2 gel, provide a physical platform for the oxide support and the supported catalyst. The support layer (TiO_2 in this work) is directly in contact with the nano-sized precious metal and can participate in the catalytic reaction *via* the support–metal interface and/or indirectly through metal–support interactions. By this definition, TiO_2(110) single crystal acts as both the substrate and the oxide support in this work, as the top few layers of the single crystal may participate in the chemical reaction and the bulk of the crystal provides a physical framework and mechanical strength.

Model catalysts Pd/TiO_2(110), Pd/TiO_2/Si(100), Pd/TiO_2/fused silica and practical catalysts Pd/TiO_2/SiO_2 gel were prepared using Pd and TiO_2 ALD, respectively. The surface area of the substrate was assumed the same before and after the ALD coating.[33,34] Their physical appearance and properties are shown in Fig. 1 and summarized in Table 1. Complexity of the catalysts increases in this order:

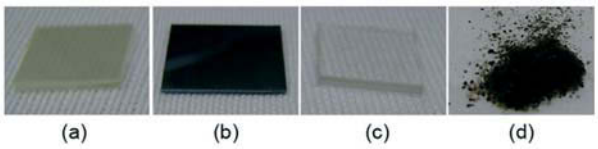

Fig. 1 Samples investigated in this work: (a) $Pd/TiO_2(110)$, (b) $Pd/TiO_2/Si(100)$, (c) Pd/TiO_2/fused silica, and (d) $Pd/TiO_2/SiO_2$ gel.

Table 1 List of supported Pd catalysts, support properties and characterization methods

Catalyst	Support (TiO_2) structure	Substrate structure	Substrate resistivity
$Pd/TiO_2(110)$	Rutile	Crystalline wafer	Semiconductor
$Pd/TiO_2/Si(100)$	—[a]	Crystalline wafer	Semiconductor
Pd/TiO_2/fused silica	—[a]	Amorphous wafer	Insulator
$Pd/TiO_2/SiO_2$ gel	—[a]	Amorphous powder	Insulator

[a] ALD TiO_2 is "invisible" to conventional XRD.

$$Pd/TiO_2(110) < Pd/TiO_2/Si(100) < Pd/TiO_2/\text{fused silica} < Pd/TiO_2/SiO_2 \text{ gel}$$

XRD was performed on all the catalysts and the XRD patterns are shown in Fig. 2. There is no specific crystalline structure for SiO_2 gel and fused silica, both of which show only a broad feature at 2θ = 20–30°. The Si(100) wafer has sharp peaks at 2θ = 33.1° and 69.3° assigned to Si(200) and Si(400), respectively.[35] The substrate crystallinity turns out to be critical for certain characterization techniques. For example, the grazing incidence XAS could not be performed on crystalline substrates which will be discussed in detail in the XAS session.

The TiO_2 thin film prepared using ALD is "invisible" to conventional XRD (see Fig. S1†). The broad diffraction feature at 2θ = 20–30° corresponding to SiO_2 decreased after TiO_2 thin film was deposited using ALD. However, no additional peak that corresponding to either rutile or anatase TiO_2 arised after TiO_2 ALD. This may be explained by one or both of the following reasons: 1) the TiO_2 film is too thin to generate enough long range order, and 2) the TiO_2 film prepared by ALD is amorphous. It was found that the TiO_2 thin film prepared at 150 °C using $TiCl_4$ and H_2O as reactants would not initiate crystallization until more than 300 cycles (equivalent to about 18 nm in thickness).[36] The thickest TiO_2 film used in this work is about 1.2 nm in thickness, seemingly too thin to start crystallization.

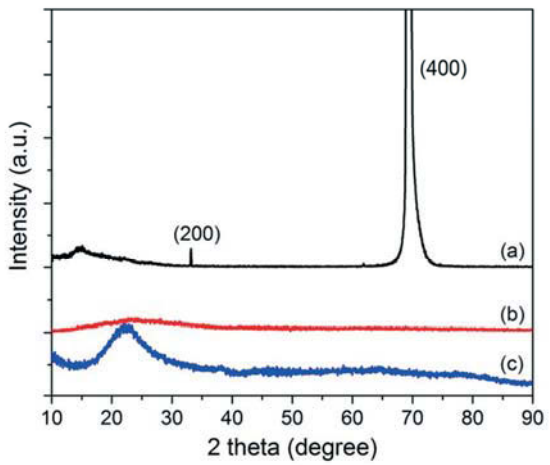

Fig. 2 XRD patterns for (a) Si(100), (b) fused silica and (c) SiO_2 gel powder.

The morphology of the as-prepared supported Pd catalysts is illustrated in Fig. 3. In Fig. 3(a), a STM image of the $Pd/TiO_2(110)$ shows dispersed Pd nanoparticles on TiO_2 terraces. Line scans were performed to obtain the height distribution 0.5 ± 0.1 nm of the Pd particles. The apparent radii obtained from STM images are oftentimes overestimated due to tip convolution effects. If the particles on the $TiO_2(110)$ surface are assumed hemispherical, the diameter of the nanoparticles is ~1 nm. There is no preferential nucleation of Pd on step edges.[26] Fig. 3(b) is a STEM image of highly dispersed Pd nanoparticles supported by TiO_2-coated SiO_2 gel. The size distribution of the Pd is about 0.9 ± 0.2 nm, similar to the diameter of the Pd nanoparticles measured on the $TiO_2(110)$ surface. The SiO_2 gel substrate was coated by 5 ALD cycles of TiO_2 which did not completely cover the SiO_2 surface. From our previous Pd ALD study, Pd deposits preferentially on the TiO_2 and not the SiO_2 surface.[27,28] This explains why the Pd particle density is slightly lower on the $Pd/TiO_2/SiO_2$ gel catalyst. Atomic force microscopy was performed on the $Pd/TiO_2/Si(100)$ model catalyst (see Fig. S2†). As 20 ALD TiO_2 cycles generates ~1.2 nm TiO_2, similar to the Pd particle size, it is difficult to distinguish between the Pd particles and the TiO_2 from AFM images. The surface roughness did not significantly change before and after the Pd ALD on the 20 cycle TiO_2-coated $SiO_2(100)$ surface.

Fig. 4 shows the Pd 3d X-ray photoelectron spectra for the Pd catalysts. The binding energies are summarized in Table 2. In both model and practical catalysts, the Pd nanoparticles were partially oxidized, showing features corresponding to Pd^0 (335.7 eV) and Pd^{2+} (337.9 eV). XPS data from the Ti-2p core states (458.5 eV) show no substantial changes on the addition of Pd nanoclusters, aside from uniform attenuation, supporting the notion of little or no

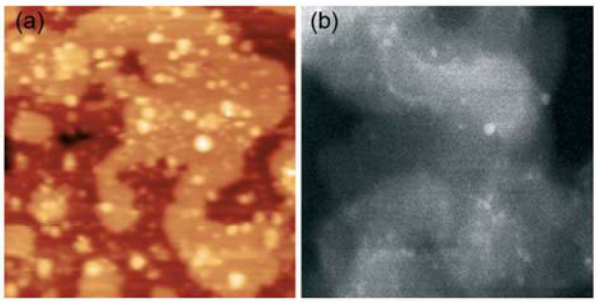

Fig. 3 (a) STM image of $Pd/TiO_2(110)$, V_{bias} = 1.3 V, I_T = 0.3 nA, 50 × 50 nm, and (b) STEM image of $Pd/TiO_2/SiO_2$ gel, 50 × 50 nm.

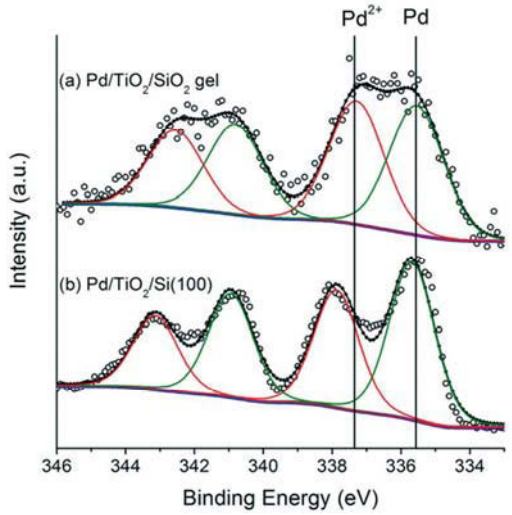

Fig. 4 X-ray photoelectron spectra of Pd 3d of as-prepared (a) practical catalyst $Pd/TiO_2/SiO_2$ gel and (b) model catalyst $Pd/TiO_2/Si(100)$. Open circle: raw data. Dotted line: sum of fittings. Olive: Pd 3d of Pd^0. Red: Pd 3d of Pd^{2+}. Energy separations for doublets were kept fixed at 5.26 eV.

nanocluster/substrate interaction. Compared with the $Pd/TiO_2/Si(100)$ model catalysts, the Pd $3d_{5/2}$ for Pd^{2+} (337.5 eV) and Ti $2p_{3/2}$ (458.2) binding energy on $Pd/TiO_2/SiO_2$ gel catalysts shifts 0.4 eV to lower binding energy. The difference in binding energies may be caused by the action of the charge neutralizer to compensate the surface charging effect during measuring the $Pd/TiO_2/SiO_2$ catalyst. There are two oxidation state associated with the Si substrate: Si^0 (99.3 eV) and Si^{4+} (102.5 eV). The presence of Si^{4+} is due to the native oxide layer on the Si(100) surface.

X-ray absorption spectroscopy (XAS) can provide information such as oxidation state and the neighboring atoms of the element of interest. XAS can be measured in transmission and/or fluorescence mode. Transmission measurement is frequently used to measure concentrated samples such as high surface area heterogeneous catalysts and gives excellent data.[38–40] For diluted samples such as the $Pd/TiO_2(110)$, $Pd/TiO_2/Si(100)$ and Pd/TiO_2/fused silica model catalysts in this work, grazing incidence XAS (GI-XAS) was employed using a fluorescence detector. However, we found that it was inherently impossible to obtain precise data for the model catalysts using a single crystal as the substrate. Even at a grazing angle, a portion of the X-ray beam was still able to penetrate the crystalline substrate and generate diffraction peaks in the EXAFS spectra, leading to poor quality data and greatly complicating the analysis (see Fig. S3†). However, the amorphous structure and optically smooth surface of the model catalysts prepared on fused silica facilitated accurate and reliable GI-XAS studies.

Table 2 Properties of the as-prepared Pd catalysts

Catalyst	Binding energy (eV)			
	Pd $3d_{5/2}$	Ti $2p_{3/2}$	Si 2p	O 1s
$Pd/TiO_2(110)$[a]	335.6	459.3	—	530.6
$TiO_2/Si(100)$	—	458.5	99.3	531.9
			102.5	530.0
$Pd/TiO_2/Si(100)$	337.9	458.6	99.8	532.0
	335.7		102.6	530.0
$Pd/TiO_2/SiO_2$ gel	337.5	458.2	103.3	532.2
	335.6			529.8

[a] Data obtained from ref. 37.

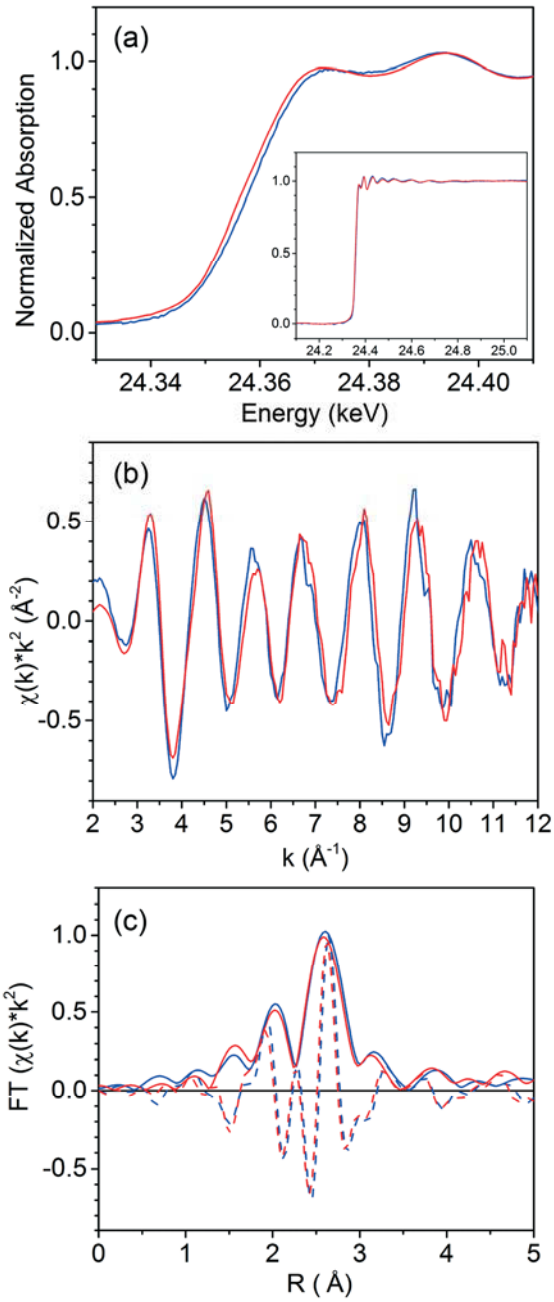

Fig. 5 XANES and EXAFS data at Pd K edge for model catalyst Pd/TiO_2/fused silica and practical catalyst $Pd/TiO_2/SiO_2$ gel. (a) XANES with inserted full range normalized XAS spectra, (b) k^2-weighted EXAFS, and (c) Fourier transform EXAFS data. Blue: Pd/TiO_2/fused silica. Red: $Pd/TiO_2/SiO_2$ gel.

The as-prepared catalysts were first reduced in 3.5% hydrogen at 523 K for 30 minutes, purged with UHP helium at

Table 3 Pd K edge EXAFS fits of the Pd catalysts after hydrogen reduction at 250 °C[a]

Catalyst	Scatter	CN_{Pd-Pd}	R (Å)	DWF ($\times 10^3$)	E_0 (eV)
Pd/TiO_2/fused silica	Pd–Pd	5.4	2.76	2.5	7.9
$Pd/TiO_2/SiO_2$ gel	Pd–Pd	5.7	2.77	2.5	7.6

[a] CN is coordination numbers with error ±10%. R is bond distance with error ±0.02 Å. DWF is Debye–Waller factor. E_0 is energy shift. A two-shell model fit of the k^2-weighted EXAFS data was obtained between k = 2.8–11.5 Å^{-1} and r = 1.3–2.8 Å. Size was estimated base on CN.

523 K for 10 minutes and finally cooled in UHP He to room temperature. Both catalysts were measured at room temperature. Fig. 5 shows Pd edge XANES and EXAFS of the Pd/TiO_2/fused silica model catalyst and the $Pd/TiO_2/SiO_2$ gel practical catalyst, measured using GI-XAS with fluorescence detector and XAS in the transmission mode, respectively. The diffraction peaks from the substrate were avoided (inset in Fig. 5(a)) because of the use of an amorphous fused silica substrate. The spectra obtained from transmission mode XAS and fluorescence mode GI-XAS are very similar. In particular, the Pd–Pd coordination number and bond-distance for the Pd/TiO_2/fused silica and $Pd/TiO_2/SiO_2$ gel determined by fitting the EXAFS data are extremely close (Table 3). The particle diameter can be estimated to be about 1 nm using the coordination number of Pd–Pd scatter,[41] consistent with the STM and STEM results.

To further understand the electronic structure and valence band of the Pd catalysts, resonant photoelectron spectroscopy was carried out using monochromotic vacuum-ultraviolet photons. Resonant photoelectron spectroscopy has been successfully applied to many systems, specifically transition metals and lanthanides to elucidate the electronic nature and hybridization behavior between cations and their surrounding oxygen ligands.[42,43] For Pd/TiO_2/Si(100), this resonance is observed as an enhancement in the Pd 4d valence band intensity as a function of photon energy from 34 to 110 eV, shown in Fig. 6. In those data, the photoemission features between 0–4 eV are primarily Pd 4d while the region between 4–10 eV arises primarily from O 2p states of the TiO_2 support. Although TiO_2 and Si contribute throughout the spectra the features between 0–4 eV are dominated by the Pd 4d support due both to a larger cross-section and physical attenuation of the underlying substrate signal. The data in Fig. 6 show that there is a clear enhancement of the Pd 4d electronic states between 60 and 90 eV photon energies. This resonance occurs due to a new channel opening up for d-electron emission: electrons excited from the filled 4p to empty 5s states can resonantly decay back into their empty core–hole with the emission of an additional 4d-electron to conserve energy. Photoemission data taken from the TiO_2/Si(100) substrate without Pd nanoclusters show similar intensity variations as seen in the data in Fig. 6 with no additional resonance features.

Fig. 7(a) illustrates the valence band spectrum taken at 82 eV shown with a background due to inelastically-scattered electrons and five Gaussian peaks, providing the fit given by the dots on the solid curve. The peaks A and B are assigned to Pd 4d bands and peaks C and D are from hybridized oxygen 2p bands of the TiO_2, consistent with the theoretical and experimental results obtained for Pd/TiO_2(110) model catalysts in the literature.[44,45] The fifth peak centered at 11 eV could be related to the carbon contamination or surface hydroxyls on the support. The intensity of peak A appearing at a binding energy of 0.65 eV is plotted as a function of photon energy in Fig. 7(b). The figure explicitly shows that this feature of Pd valence band is strongly resonant at the Pd 4p threshold. It

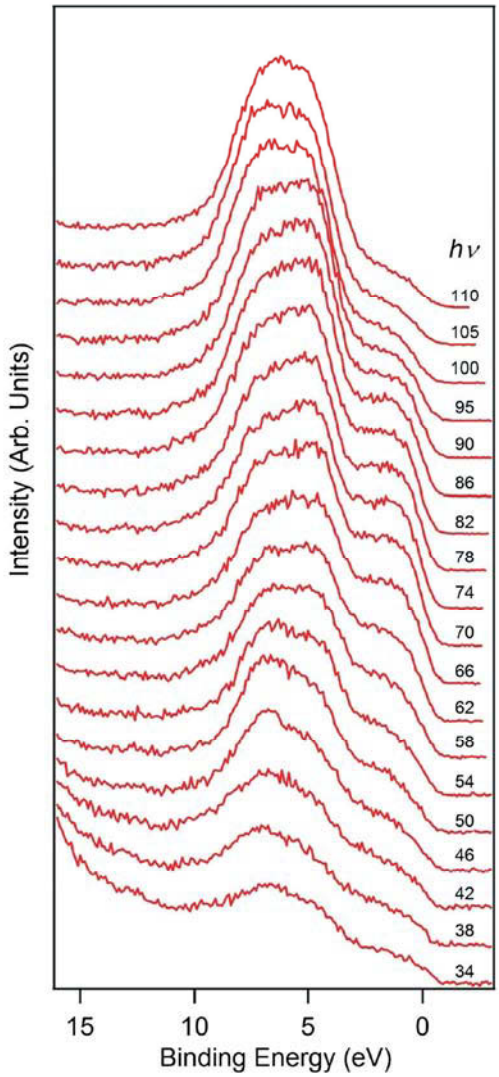

Fig. 6 The valence band of the Pd/TiO_2/Si(100) acquired varying the photon energy from 34 to 110 eV.

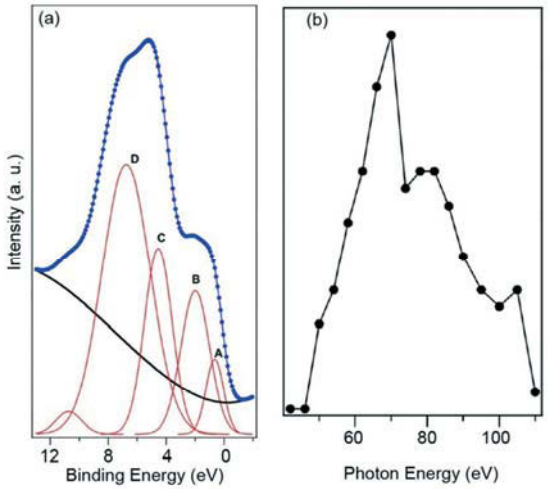

Fig. 7 (a) The valence band of the Pd/TiO_2/Si(100) acquired with photon energy of 82 eV and its fitting curve and the convoluting peaks, (b) intensity of the Pd 4d band as a function of the photon energy.

has been reported that as the particle size of metal clusters decreases, due to changes in bond length and the coordination, the electronic structure of metal clusters is also altered and is different from their bulk counterpart. The small size effect leads to an increase of d-hole population in metal clusters.[46] Clusters with d-holes would be metallic, however, and since we do not see a sharp Fermi edge, we do not have substantial charge transfer out of the clusters. Filled 4d levels suggest that there is little charge transfer from the Pd clusters and only weak interactions with the TiO_2/Si(100) substrate, consistent with the XPS data. Pd/TiO_2/SiO_2 gel was not characterized using RPES due to the insulating nature of the SiO_2 gel substrate. There would be a charging effect, causing the peaks and valence band to shift in an unpredictable manner.

Conclusions

In conclusion, we used ALD to prepare a series of model and practical Pd catalysts, including Pd/TiO_2(110), Pd/TiO_2/Si(100), Pd/TiO_2/fused silica, and Pd/TiO_2/SiO_2 gel. Particularly, the last three types of catalysts were synthesized in the ALD chamber simultaneously. The resultant catalysts exhibited similar local geometric and electronic structure. Both STM and STEM showed that the Pd nanoparticles were ~1 nm in diameter. XPS revealed that Pd nanoparticles in both model and practical catalysts were partially oxidized upon exposing to ambient conditions. Grazing incidence XAS in fluorescence mode was used to measure the model catalysts, while XAS in transmission mode was employed to the high surface area powder catalysts. The fitting to the *in situ* XAS data showed that both Pd nanocatalysts exhibited extremely similar Pd–Pd coordination number and bond distance, indicating similar Pd particle size and chemical environment. The resonance of the Pd 4d valence band as a function of photon energy was observed using RPES. Little charge transfer from the Pd nanoparticles to TiO_2 indicated weak metal–support interactions, consistent with the XAS and XPS results from both model and practical catalysts.

ALD is a promising, alternative synthesis method to prepare heterogeneous catalysts in both model and practical systems. Owing to the nature of the self-limiting surface reactions, it allows conformal deposition of nanoparticles and thin film on both planar and high surface area substrates at the same time in one batch. While the appearance of the catalysts may look dramatically different, the chemical environmental of the model and practical catalysts prepared by ALD could be identical to each other. This unique property could aid in bridging the "synthesis gap" between the model and practical catalysts and ultimately will lead to discoveries of better catalysts.

Acknowledgements

This material is based upon work supported as part of the Institute for Atom-efficient Chemical Transformations (IACT), an Energy Frontier Research Center funded by the U.S. Department of Energy, Office of Science, Office of Basic Energy Sciences. ZL and YL thank the National Science Foundation (CBET-1511820) for financial support. Use of the Advanced Photon Source was supported by the U. S. Department of Energy, Office of Science, Office of Basic Energy Sciences, under Contract No. DE-AC02-06CH11357. MRCAT operations are supported by the Department of Energy and the MRCAT member institutions. Use of the Center for Nanoscale Materials was supported by the U. S. Department of Energy, Office of Science, Office of Basic Energy Sciences, under Contract No. DE-AC02-06CH11357.

References

1 D. G. Castner, B. A. Sexton and G. A. Somorjai, *Surf. Sci.*, 1978, **71**, 519–540.
2 R. Imbihl and G. Ertl, *Chem. Rev.*, 1995, **95**, 697–733.
3 M. Baumer and H. J. Freund, *Prog. Surf. Sci.*, 1999, **61**, 127–198.
4 D. W. Goodman, *Chem. Rev.*, 1995, **95**, 523–536.
5 C. T. Campbell, *Surf. Sci. Rep.*, 1997, **27**, 1–111.
6 C. R. Henry, *Surf. Sci. Rep.*, 1998, **31**, 235–325.
7 M. S. Chen, D. Kumar, C. W. Yi and D. W. Goodman, *Science*, 2005, **310**, 291–293.
8 Y. N. Sun, Z. H. Qin, M. Lewandowski, E. Carrasco, M. Sterrer, S. Shaikhutdinov and H. J. Freund, *J. Catal.*, 2009, **266**, 359–368.
9 S. M. Lang and T. M. Bernhardt, *Phys. Chem. Chem. Phys.*, 2012, **14**, 9255–9269.
10 W. Yu, M. D. Porosoff and J. G. Chen, *Chem. Rev.*, 2012, **112**, 5780–5817.
11 S. Vajda and M. G. White, *ACS Catal.*, 2015, **5**, 7152–7176.
12 *Model Systems in Catalysis: Single Crystals to Supported Enzyme Mimics*, ed. R. M. Rioux, Springer, 2009.

13 M. Flytzani-Stephanopoulos and B. C. Gates, in *Annu. Rev. Chem. Biomol. Eng.*, ed. J. M. Prausnitz, 2012, vol. 3, pp. 545–574.
14 S. D. Senanayake, D. Stacchiola and J. A. Rodriguez, *Acc. Chem. Res.*, 2013, **46**, 1702–1711.
15 H. F. Wang, H. Ariga, R. Dowler, M. Sterrer and H. J. Freund, *J. Catal.*, 2012, **286**, 1–5.
16 F. Ringleb, M. Sterrer and H. J. Freund, *J. Catal.*, 2014, **474**, 186–193.
17 B. J. O'Neill, D. H. K. Jackson, J. Lee, C. Canlas, P. C. Stair, C. L. Marshall, J. W. Elam, T. F. Kuech, J. A. Dumesic and G. W. Huber, *ACS Catal.*, 2015, **5**, 1804–1825.
18 T. D. Gould, A. M. Lubers, A. R. Corpuz, A. W. Weimer, J. L. Falconer and J. W. Medlin, *ACS Catal.*, 2015, **5**, 1344–1352.
19 Y. Wu, Z. Lu, L. Emdadi, S. C. Oh, J. Wang, Y. Lei, H. Chen, D. T. Tran, I. C. Lee and D. Liu, *J. Catal.*, 2016, **337**, 177–187.
20 F. Zaera, *J. Phys. Chem. Lett.*, 2012, **3**, 1301–1309.
21 S. M. George, *Chem. Rev.*, 2010, **110**, 111–131.
22 A. C. Kozen, C.-F. Lin, A. J. Pearse, M. A. Schroeder, X. Han, L. Hu, S.-B. Lee, G. W. Rubloff and M. Noked, *ACS Nano*, 2015, **9**, 5884–5892.
23 Y. Lei, F. Mehmood, S. Lee, J. Greeley, B. Lee, S. Seifert, R. E. Winans, J. W. Elam, R. J. Meyer, P. C. Redfern, D. Teschner, R. Schlogl, M. J. Pellin, L. A. Curtiss and S. Vajda, *Science*, 2010, **328**, 224–228.
24 J. L. Lu, B. S. Fu, M. C. Kung, G. M. Xiao, J. W. Elam, H. H. Kung and P. C. Stair, *Science*, 2012, **335**, 1205–1208.
25 L. F. Hakim, J. A. McCormick, G.-D. Zhan, A. W. Weimer, P. Li and S. M. George, *J. Am. Ceram. Soc.*, 2006, **89**, 3070–3075.
26 Y. Lei, B. Liu, J. L. Lu, X. Lin, L. Gao, N. Guisinger, J. P. Greeley and J. W. Elam, *Phys. Chem. Chem. Phys.*, 2015, **17**, 6470–6477.
27 Y. Lei, B. Liu, J. Lu, J. A. Libera, J. P. Greeley and J. W. Elam, *J. Phys. Chem. C*, 2014, **118**, 22611–22619.
28 Y. Lei, J. L. Lu, H. Y. Zhao, B. Liu, K. B. Low, T. P. Wu, J. A. Libera, J. P. Greeley, P. J. Chupas, J. T. Miller and J. W. Elam, *J. Phys. Chem. C*, 2013, **117**, 11141–11148.
29 J. W. Elam, M. D. Groner and S. M. George, *Rev. Sci. Instrum.*, 2002, **73**, 2981–2987.
30 J. W. Elam, A. Zinovev, C. Y. Han, H. H. Wang, U. Welp, J. N. Hryn and M. J. Pellin, *Thin Solid Films*, 2006, **515**, 1664–1673.
31 D. Friebel, D. J. Miller, C. P. O'Grady, T. Anniyev, J. Bargar, U. Bergmann, H. Ogasawara, K. T. Wikfeldt, L. G. M. Pettersson and A. Nilsson, *Phys. Chem. Chem. Phys.*, 2011, **13**, 262–266.
32 S. J. A. Figueroa, S. J. Stewart, T. Rueda, A. Hernando and P. de la Presa, *J. Phys. Chem. C*, 2011, **115**, 5500–5508.
33 J. W. Elam, J. A. Libera, T. H. Huynh, H. Feng and M. J. Pellin, *J. Phys. Chem. C*, 2010, **114**, 17286–17292.
34 J. L. Lu, K. M. Kosuda, R. P. Van Duyne and P. C. Stair, *J. Phys. Chem. C*, 2009, **113**, 12412–12418.
35 C.-K. Jung, B.-C. Kang, H.-Y. Chae, Y.-S. Kim, M.-K. Seo, S.-K. Kim, S.-B. Lee, J.-H. Boo, Y.-J. Moon and J.-Y. Lee, *J. Cryst. Growth*, 2002, **235**, 450–456.
36 J. Aarik, A. Aidla, H. Mandar and T. Uustare, *Appl. Surf. Sci.*, 2001, **172**, 148–158.
37 A. Gharachorlou, M. D. Detwiler, A. V. Nartova, Y. Lei, J. L. Lu, J. W. Elam, W. N. Delgass, F. H. Ribeiro and D. Y. Zemlyanov, *ACS Appl. Mater. Interfaces*, 2014, **6**, 14702–14711.
38 Y. Lei, H. Y. Zhao, R. Diaz-Rivas, S. Lee, B. Liu, J. L. Lu, E. A. Stach, R. E. Winans, K. W. Chapman, J. P. Greeley, J. T. Miller, P. J. Chupas and J. W. Elam, *J. Am. Chem. Soc.*, 2014, **136**, 9320–9326.
39 Y. Lei, J. Jelic, L. C. Nitsche, R. Meyer and J. T. Miller, *Top. Catal.*, 2011, **54**, 334–348.
40 S. Bordiga, E. Groppo, G. Agostini, J. A. van Bokhoven and C. Lamberti, *Chem. Rev.*, 2013, **113**, 1736–1850.
41 A. I. Frenkel, C. W. Hills and R. G. Nuzzo, *J. Phys. Chem. B*, 2001, **105**, 12689–12703.
42 U. Diebold, H. S. Tao, N. D. Shinn and T. E. Madey, *Phys. Rev. B*, 1994, **50**, 14474–14480.
43 T. Kaurila, J. Vayrynen and M. Isokallio, *J. Phys.: Condens. Matter*, 1997, **9**, 6533–6542.
44 J. Zhang and A. N. Alexandrova, *J. Chem. Phys.*, 2011, **135**, 174702.
45 M. D. Negra, N. M. Nicolaisen, Z. Li and P. J. Moller, *Surf. Sci.*, 2003, **540**, 117–128.
46 P. Zhang and T. K. Sham, *Phys. Rev. Lett.*, 2003, **90**, 245502.